Research Article

Nano Research
2021, 14(3): 788–796

ISSN 1998-0124 CN 11-5974/O4
https://doi.org/10.1007/s12274-020-3217-7

De novo synthesis of bifunctional conjugated microporous polymers for synergistic coordination mediated uranium entrapment

Boxuan Yu[1,2,3,§], Lei Zhang[1,4,§], Gang Ye[1,5] (✉), Qingzhi Liu[4,6], Jiongli Li[2,3], Xudong Wang[2,3], Jing Chen[1,5], Shengming Xu[1,5] (✉), and Shengqian Ma[4,†] (✉)

[1] *Collaborative Innovation Center of Advanced Nuclear Energy Technology, Institute of Nuclear and New Energy Technology, Tsinghua University, Beijing 100084, China*
[2] *Beijing Institute of Graphene Technology, Beijing 100094, China*
[3] *Beijing Institute of Aeronautical Materials, Beijing 100085, China*
[4] *Department of Chemistry, University of South Florida, 4202 E. Fowler Avenue, Tampa, FL 33620, USA*
[5] *Beijing Key Lab of Radioactive Waste Treatment, Tsinghua University, Beijing 100084, China*
[6] *College of Chemistry and Pharmaceutical Sciences, Qingdao Agricultural University, Qingdao 266109, China*
[†] *Present address: Department of Chemistry, University of North Texas, 1508 W. Mulberry St, Denton, TX 76201, USA*
[§] *Boxuan Yu and Lei Zhang contributed equally to this work.*

Received: 7 September 2020 / **Revised:** 19 October 2020 / **Accepted:** 29 October 2020

ABSTRACT

This work reports a *de novo* synthesis of novel bifunctional conjugated microporous polymers (CMPs) exhibiting a synergistic-effect involved coordination behavior to uranium. It is highlighted that the synthetic strategy enables the engineering of the coordination environment within amidoxime functionalized CMP frameworks by specifically introducing *ortho*-substituted amino functionalities, enhancing the affinity to uranyl ions via forming synergistic complexes. The CMPs exhibit high Brunauer–Emmett–Teller (BET) surface area, well-developed three-dimensional (3D) networks with hierarchical porosity, and favorable chemical and thermal stability because of the covalently cross-linked structure. Compared with the amino-free counterparts, the adsorption capacity of bifunctional CMPs was increased by almost 70%, from 105 to 174 mg/g, indicating evidently enhanced binding ability to uranium. Moreover, new insights into coordination mechanism were obtained by in-depth X-ray photoelectron spectroscopy (XPS) analysis and density functional theory (DFT) calculation, suggesting a dominant role of the oxime ligands forming a 1:1 metal ions/ligands (M/L) coordination model with uranyl ions while demonstrating the synergistic engagement of the amino functionalities via direct binding to uranium center and hydrogen-bonding involved secondary-sphere interaction. This work sheds light on the underlying principles of *ortho*-substituted functionalities directed synergistic effect to promote the coordination of amidoxime with uranyl ions. And the synthetic strategy established here would enable the task-specific development of more novel CMP-based functional materials for broadened applications.

KEYWORDS

conjugated microporous polymers, uranium, adsorption, synergistic coordination, density functional theory

1 Introduction

Conjugated microporous polymers (CMPs) are a series of macromolecules with π-conjugated three-dimensional (3D) networks consisting of building blocks via covalent bonds [1, 2]. Since the first synthesis of CMPs by Sonogashira-Hagihara coupling [3] of halogen and alkyne monomers in 2007 [4], CMPs have emerged as one of the most promising materials applied in many fields [5, 6], including luminescent materials [7, 8], heterogeneous catalysis [9, 10], energy storage [11–13], environmental remediation [14–16] and, particularly, removal of heavy metal ions [17, 18]. CMPs generally show advantages in terms of task-specific designability [19], benign synthesis, and controlled porosity [20]. Due to the unique π-conjugated covalent structure, these fascinating materials exhibit superior structural and chemical stability compared to most of the members in the family of organic porous materials [21]. Moreover, the well-folded skeletons of CMPs are similar to natural protein scaffolds that have evolved over millennia to chelate specific metal ions with high selectivity [22]. These intriguing properties endow CMPs with great potential to be engineered as high-efficiency separation materials for entrapment of heavy metal ions [23].

Among all types of heavy metal ion contaminants, uranyl ions, the predominant species of uranium in aqueous environments, draw great attention due to their high environmental toxicity and strategic value after recovery [24]. On one hand, excessive uranyl ions in environmental water would cause serious radioactive sickness, such as DNA damage and cancer, to human beings and other creatures [25]. On the other hand,

Address correspondence to Gang Ye, yegang@mail.tsinghua.edu.cn; Shengming Xu, smxu@tsinghua.edu.cn; Shengqian Ma, Shengqian.Ma@unt.edu

as a strategic resource, considerable amounts of uranium from ocean water and radioactive wastes is a kind of alternative source to traditional mines, especially for the uranium-scarce countries [26]. Thus, it is crucial to develop advanced adsorption materials to separate uranyl ions from water in a cost- and energy-efficient way.

CMPs with rational design or modification are considered as promising sorbents to address this challenge [27]. For the entrapment of uranyl ions, a universally accepted strategy for sorbent synthesis is to endow substrates with specific functional groups that provide additional interactions, such as hydrogen bond interactions [28] or coordination [29]. In this regard, substantial efforts have been devoted to the synthesis of CMPs from monomers containing different functionalities [30, 31], or the post-modification of intrinsic CMPs by introducing different ligands [18, 32]. Among the known functional groups, amidoxime, usually converted from nitriles, stands out because of its high affinity and specificity toward uranium under neutral and slightly alkaline conditions [33–35]. Such affinity can be ascribed to the rearrangement of protons in oxime group and the deprotonation in imide group, which results in a conjugated system with delocalized electron density to trap uranyl ions by in-plane coordination [36, 37]. Several theories have been proposed to describe the coordination mechanism of amidoxime with uranyl ions [38, 39], among which the cooperative binding involving the two adjacent amidoximes and cyclic imide dioxime binding are the most prevailing modes [40]. However, for CMP-based sorbents bearing amidoxime groups, the classic cooperative binding mode is difficult to be achieved due to the rigid skeleton and discrete amidoxime distribution in the pore channels. In our recent work, a bis-amidoxime-functionalized homo-coupled CMP was developed by the addition reaction of diyne units with malononitrile, enabling effective adsorption of uranyl ions via cooperative binding [41]. The post-modification strategy did not afford a controllable conversion of nitrile groups to amidoxime functionalities within the microporous CMP frameworks [29]. Besides, computational studies showed a high relative free energy change (ΔG_{rel}) for the cooperative binding of bis-amidoxime substituted at the same position to uranyl ions, resulting in a moderate capacity for uranium separation [42, 43].

Introducing neighboring functionalities such as amino [44] and carboxyl [45] to establish the synergistic effect represents another promising strategy to enhance the binding ability of amidoxime groups to uranyl ions. In this respect, a prerequisite for sorbent development is to effectively create synergistic functionalities located adjacent to amidoxime groups by task-specific synthesis which allows the formation of synergistic binding to uranyl ions. This remains a considerable challenge for conventional synthetic strategies such as copolymerization, grafting, or post-modification [46–48], especially within the confined pore channels of CMP-based sorbents.

To overcome this limitation, herein, we report a facile and effective *de novo* synthetic strategy to engineer the coordination environment of amidoxime-functionalized CMPs by establishing well-defined synergistic binding sites for efficient entrapment of uranyl ions. The classic Sonogashira-Hagihara coupling of phenylacetylene with bromobenzene was employed as a model reaction to construct the basic skeletons of CMPs, imparting the sorbents with favorable porosities and stabilities [4, 49]. Given the ability of electron-donating and the strong tendency to form hydrogen bonding [50], amino was selected as a synergistic group to amidoxime, which was specifically introduced to the *ortho*-position by the *de novo* synthesis using 2-amino-3,5-dibromobenzonitrile as a bifunctional monomer. Transforming the cyano to amidoxime groups by hydroxylamine treatment resulted in the target CMP sorbent CMP-mAO-oNH$_2$ (Scheme 1). Native amidoxime functionalized counterpart CMP-mAO without the neighboring amino groups was also synthesized for a comparative study. It is highlighted that, due to the synergistic binding effect of the *ortho*-substituted amino functionalities, CMP-mAO-oNH$_2$ presented significantly increased adsorption capacity for uranyl ions compared to CMP-mAO. Moreover, in-depth X-ray photoelectron spectroscopy (XPS) analysis and density functional theory (DFT) calculation were employed to explore the coordination mechanism. New insights into the amino-involved synergistic coordination were obtained, revealing a 1:1 metal ions/ligands (M/L) coordination model stabilized by the electron-donating amino functionalities directly coordinating to the uranyl center as well as the hydrogen bonding involved secondary-sphere interaction.

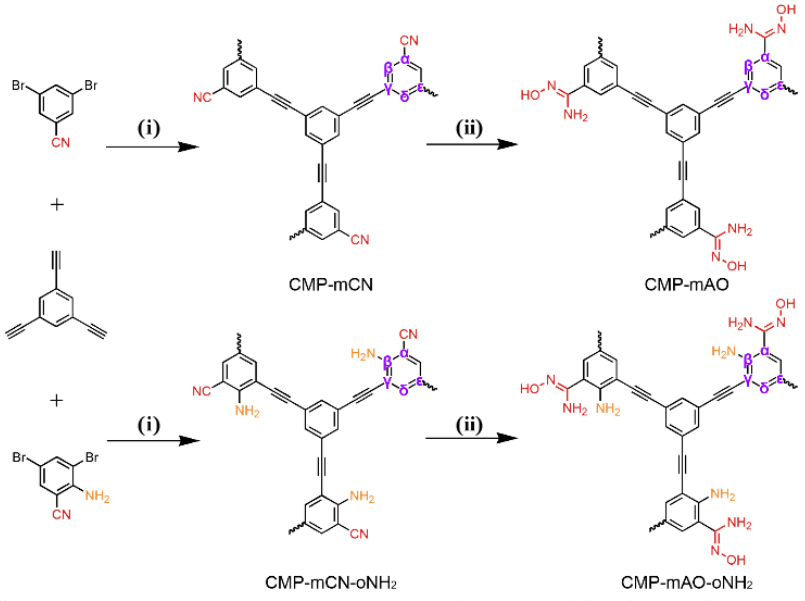

Scheme 1 Synthetic route of CMPs-mAO and CMPs-mAO-oNH$_2$, reagent: (i) bis-(triphenylphosphine) palladium(II) dichloride, CuI, TEA, DMF; (ii) NH$_2$OH·HCl, TEA, DMF.

2 Experimental

2.1 Materials

3,5-Dibromobenzonitrile (98%), 2-amino-3,5-dibromobenzonitrile (99%), bis-(triphenylphosphine) palladium(II) dichloride (98%), copper(I) iodide (99.9%), triethylamine (TEA, 99%), N,N-dimethylformamide (DMF, 99.8%, SuperDry, J&K Seal), arsenazo III (95%[t], spectrophotometric reagent for U, Th, Zr and other metals, indicator for the precipitation titration of SO_4 with Ba) and L-(+)-tartaric acid (99%) were purchased from J&K Scientific LTD. 1,3,5-Triethynylbenzene (98%) was purchased from EXTENSION Scientific LTD. Hydroxylamine hydrochloride (99%) was purchased from Sigma-Aldrich. Chloroform (99.5%, AR), methanol (99%, AR), nitric acid (69%), potassium hydroxide (95%), and sodium hydroxide (99%) were purchased from Beijing Chemical Works. Deionized water used in adsorption tests was purchased from WATSONS. Uranyl nitrate hexahydrate ($UO_2(NO_3)_2{\cdot}6H_2O$) was provided by the China Institute of Atomic Energy (CIAE). All reagents were used as received without further purification.

2.2 Preparation of CMP-mCN and CMP-mCN-oNH$_2$

CMP-mCN and CMP-mCN-oNH$_2$ were synthesized through a modified process according to a previous report [51]. Taking CMP-mCN as an example, 1,3,5-triethynylbenzene (1.5 mmol, 225 mg), 3,5-dibromobenzonitrile (1.5 mmol, 391 mg), bis-(triphenylphosphine) palladium(II) dichloride (0.075 mmol, 53 mg), and copper iodide (0.1125 mmol, 21 mg) were charged in a Schlenk flask, where a 1.5 times excess of ethynyl monomers was used to ensure porosity [52]. Then, 30 mL anhydrous DMF and 9 mL anhydrous TEA were added under the argon protection. The reaction mixture was heated at 80 °C for 2 days with magnetic stirring under argon and then cooled to room temperature. The precipitate was separated by filtration and washed three times with chloroform, water, and methanol to remove the unreacted monomer and residual catalyst. After further washed by Soxhlet extraction in methanol for 1 day and dried in vacuum for 12 h at 50 °C, CMP-mCN was obtained as brown powder. For preparation of CMP-mCN-oNH$_2$, 2-amino-3,5-dibromobenzonitrile (1.5 mmol, 414 mg) was used in reaction following the same procedure.

2.3 Preparation of CMP-mAO and CMP-mAO-oNH$_2$

As a typical synthesis recipe, 200 mg of CMP-mCN was dispersed in 20 mL of methanol, followed by the addition of 500 mg of $NH_2OH{\cdot}HCl$ and 750 mg of TEA. After being stirred at 70 °C for 48 h, the nitriles were all converted into amidoxime. Then the mixture was filtered, washed with excess methanol, and finally dried at 50 °C under vacuum. The CMP-mAO was obtained as a brown powder. For the preparation of CMP-mAO-oNH$_2$, 215 mg of CMP-mCN-oNH$_2$ was used following the same procedure.

2.4 Characterizations

Fourier transform infrared (FT-IR) spectra were recorded on Bruker Vertex 70. ^{13}C (125 MHz) cross-polarization magic-angle spinning (CP-MAS) NMR experiments were recorded on a Bruker Advance 500 spectrometer equipped with a magic-angle spin probe in a 4-mm ZrO_2 rotor. Surface chemistry and composition analysis of the samples were examined with a model 250XI XPS spectrometer equipped with a mono Al Kα X-ray source (1,361 eV). Binding energy calibration was based on C 1s at 284.6 eV. The data were analyzed using the XPSPEAK software and all high-resolution spectra were fitted with Shirley's background and a Lorentzian–Gaussian convoluted function. Organic elemental analysis was performed on an Elementar Vario EL III instrument. Nitrogen sorption isotherms were measured at 77 K on NOVA 3200e Surface Area & Pore Size Analyzer. Before measurement, the samples were degassed in vacuum at 120 °C for 3 h. The Brunauer–Emmett–Teller (BET) method was utilized to calculate the specific surface areas. Scanning electron microscopy (SEM) was conducted by using Hitachi SU 1510 and SU 4800 scanning electron microscope. Samples were deposited with metal or carbon spraying before observation. It was observed at an accelerating voltage of 30 kV in vacuum condition after metal spraying. Thermogravimetric analysis (TGA) was conducted on a TA Instruments SDT Q600 instrument at a heating rate of 10 °C/min from 50 to 1,000 °C. Samples weighing ~ 5 mg were heated in a N_2 flow (100 mL/min).

2.5 Uranium adsorption

Before adsorption experiments, all samples were treated with 3 wt.% potassium hydroxide solution for 24 h to facilitate deprotonation of amidoxime [53]. Adsorption of uranium by CMPs was implemented by batch operation in Erlenmeyer flask. Typically, a certain amount of CMPs were mixed with uranium solution, followed by magnetic stirring at room temperature. The initial pH value of the uranium solutions was adjusted by adding HNO_3 or NaOH aqueous solutions (negligible volume). The ionic strength of the solutions was maintained using 0.01 mol/L $NaClO_4$. When adsorption equilibrium was reached, the adsorbents were separated through a 0.22-μm membrane filter. The concentration of uranium solutions was determined by a UV spectrophotometer assisted by arsenazo III coloration method. Different concentrations of uranium solutions at 0, 1, 2, 4, and 5 ppm were prepared to determine the standard curve.

Adsorption capacity q (mg/g) is defined as follows

$$q = \frac{C_0 - C_e}{m} \times V \tag{1}$$

where C_0 (mg/L) and C_e (mg/L) are the initial and residual uranium concentration in the aqueous solutions, respectively, V is the volume of the initial solution and m is the weight of the CMP sorbents.

2.6 Density functional theory calculation

The coordination mode and interaction energy between uranyl ions and functional moieties were studied by DFT using the Gaussian 09 code. The expanded boundless material limits the use of accurate quantum chemistry approaches. However, the amidoxime and *ortho*-amino functional moiety distribute separately on the expanded material, making it appropriate to model the interaction between the single moiety with uranyl ions, including the coordination mode, interaction energy, and the synergistic effect. The structures of each possible coordination mode, the uranyl hydrated ions, and the representative *ortho*-amino-benzamidoxime ligand anion were optimized fully at the B3LYP level. The 5f-in-core ECP78MWB and associated valence basis set was used for U. The LANL2DZ basis set was used for C, H, O, and N atoms. For each optimized structure, analytical frequencies were calculated to ensure that the local minimum point on the potential energy surface was found. Solvent effects were taken into account implicitly with the SMD model.

3 Results and discussion

To investigate the synergistic effect on the binding ability of

CMP sorbents to uranyl ions, amidoxime functionalized CMPs with *ortho*-substituted amino groups were developed by a *de novo* synthetic strategy illustrated in Scheme 1. Firstly, CMP-mCN-oNH$_2$ was synthesized via the Pd(II)/Cu(I) catalyzed Sonogashira-Hagihara coupling of 1,3,5-triethynylbenzene and 2-amino-3,5-dibromobenzonitrile, resulting in a porous and stable conjugated skeleton. Then, hydroxylamine treatment was conducted to convert the cyano groups into amidoxime, giving the functionalized sorbent CMP-mAO-oNH$_2$. The amino groups introduced by the *de novo* synthesis located precisely at the *ortho*-position to amidoxime, which are expected to establish synergistic binding to uranyl ions. A counterpart without the amino group, CMP-mAO, was also synthesized for a comparative study by using 3,5-dibromobenzonitrile as monomers following the same procedure.

Evidence is provided in Fig. 1 to prove the successful synthesis of CMPs and the conversion of amidoxime. In the FT-IR spectra (Fig. 1(a)), the nitrile CMP precursors, labeled as CMP-mCN and CMP-mCN-oNH$_2$, show a sharp characteristic peak at 2,225 cm^{-1} corresponding to the stretching vibration of cyano groups (C≡N). After the amidoximation, the C≡N peak disappears and a weak broad peak shows up at 2,196 cm^{-1}, which is attributed to the stretching vibration of alkynyl (C≡C). Meanwhile, the resulting amidoxime-functionalized CMPs, i.e. CMP-mAO and CMP-mAO-oNH$_2$, exhibit characteristic bands in the spectral region of 937, 1,381, and 1,654 cm^{-1} assigned to the stretching of N–O, C–N, and C=N of amidoxime groups [54], indicating the effective conversion of cyano to amidoxime.

Solid-state ^{13}C-NMR was employed to examine the chemical structure of CMPs before and after amidoximation. According to the ^{13}C-NMR spectra in Fig. 1(b), the peak at 90 ppm and peaks group around 120 to 150 ppm are attributed to the alkynyl carbon (C_{al}) and aromatic carbon (C_{ar}) species in CMPs skeleton, respectively. The CMP-mCN sample shows a peak at 114.4 ppm corresponding to the overlapped signals of nitrile carbon (C_{CN}) and α carbon ($C_α$) in aromatic ring (indicated in Scheme 1). After the hydroxylamine treatment, with the conversion of electron-withdrawing nitrile to amidoxime, the $C_α$ peak of CMP-mAO shifts back into C_{ar} peaks group. Meanwhile, C_{CN} peak disappears and C_{AO} peak shows up at 152.8 ppm, suggesting the complete conversion of nitrile to amidoxime. As for CMP-mCN-oNH$_2$, with the introduction of electron-donating amino groups, the $C_α$ peak further shifts to 96.7 ppm as well as the $C_β$, $C_γ$ and $C_ε$ peaks also shift out from C_{ar} peaks group to 149.3 ppm ($C_β$) and around 100.5 ppm ($C_γ$, $C_ε$), covering the C_{CN} peak at same chemical shift. The intensity reduction of the peak at 100.5 ppm and the appearance of amidoxime group at 153.3 ppm confirm the successful amidoximation.

To confirm the elemental composition of CMPs, XPS analysis and elemental analysis were performed. Figure 1(c) gives the wide scan XPS spectra, presenting C 1s, N 1s, and O 1s signals in all CMPs samples. The O 1s signal at around 533 eV in nitrile CMPs should be attributed to the bound water molecules or other oxygen-containing impurities, the intensity of which is increased after amidoximation due to the generation of oxime. The XPS and element analysis data summarized in Table 1 both show that the molecular ratio of nitrogen to carbon (N/C molar ratio) is increased with introduction of amino groups as well as conversion of nitrile to amidoxime, which is in good agreement with the theoretical values suggesting an amidoxime content of about 20 wt.%.

The composition and structure of functional groups in CMPs were examined by a detailed analysis of the XPS spectra. High-resolution N 1s regions with deconvolution analysis in Fig. 2(a) present the transformation of N species in CMPs along with amidoximation. The N 1s regions were fit with three main components assigned to nitrile nitrogen (≡N, 399.2 eV), primary amine (–NH$_2$, 399.6 eV), and tertiary amine (=N–, 400.0 eV) functionalities. The contents of corresponding N species were summarized in Table 2. The dominant N component in CMP-mCN is ≡N species which is in accordance with previous reports [55]. After hydroxylamine treatment, all ≡N species are replaced by –NH$_2$ and =N– species, indicating the complete conversion of cyano to amidoxime. These two species show a similar amount (Table 2). The slight excess of =N– species can be attributed to the isomerization of amidoxime [56]. With the introduction of *ortho*-amino, the N 1s region of CMP-mCN-oNH$_2$ presents the overlapping of almost the same amount of ≡N and –NH$_2$ species while CMP-mAO-oNH$_2$ shows more component of –NH$_2$ to =N– species, which is in accordance with the expected structure of CMPs illustrated in

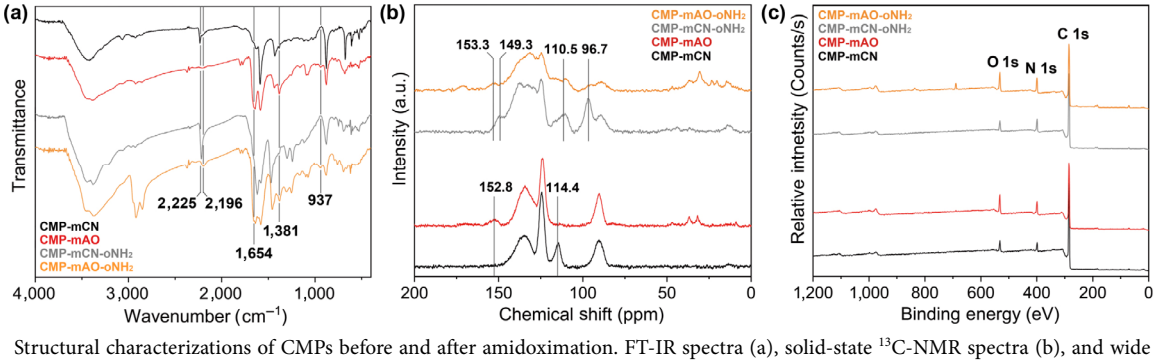

Figure 1 Structural characterizations of CMPs before and after amidoximation. FT-IR spectra (a), solid-state ^{13}C-NMR spectra (b), and wide scan XPS spectra (c) of CMP-mCN (black), CMP-mCN-oNH$_2$ (gray), CMP-mAO (red), and CMP-mAO-oNH$_2$ (orange), respectively.

Table 1 Elemental analysis of CMPs before and after amidoximation

Samples	Organic elemental analysis				XPS elemental analysis				Theoretical value
	C wt.%	N wt.%	H wt.%	N/C molar ratio	C at.%	N at.%	O at.%	N/C molar ratio	N/C molar ratio
CMP-mCN	83.0	5.30	3.38	0.0548	88.6	6.08	5.16	0.0686	0.0526
CMP-mAO	71.4	8.50	4.44	0.1020	79.8	10.5	9.65	0.1315	0.1053
CMP-mCN-oNH$_2$	74.7	8.85	3.77	0.1016	84.6	9.62	5.78	0.1137	0.1053
CMP-mAO-oNH$_2$	64.6	10.39	4.56	0.1379	77.7	12.4	9.79	0.1590	0.1579

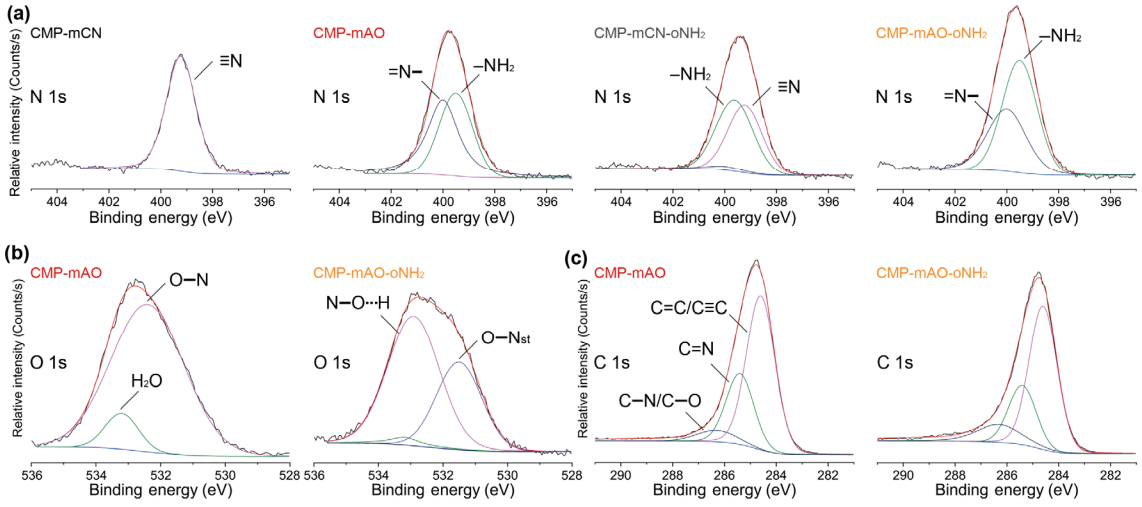

Figure 2 High-resolution XPS spectra. N 1s regions for CMPs before and after amidoximation (a); O 1s (b) and C 1s (c) regions for CMPs after amidoximation.

Table 2 XPS analysis of the N 1s species and content of CMPs before and after amidoximation

Sample	Nitrogen species (%)		
	≡N, 399.2 eV	–NH_2, 399.6 eV	=N–, 400.0 eV
CMP-mCN	99.9	—	—
CMP-mAO	—	45.9	54.1
CMP-mCN-oNH_2	45.8	50.4	3.7
CMP-mAO-oNH_2	0.8	59.0	40.3

Scheme 1. The O 1s and C 1s regions of amidoxime CMPs were also deconvoluted to explain the impact of *ortho*-amino to amidoxime. As showed in Fig. 2(b), the O 1s region of CMP-mAO can be assigned to the dominant O–N (532.4 eV) species of oxime group overlaid with a minor component of H_2O (533.2 eV) species. While with the impact of *ortho*-amino in CMP-mAO-oNH_2, the dominant O–N species were disproportionated into two states. It can be interpreted as the intramolecular hydrogen bond formed by the rearrangement of protons in amidoxime group was stabilized by the electron-donating *ortho*-amino (Fig. S1(a) in the Electronic Supplementary Material (ESM)), resulting in a relatively stable spatial structure for one part of ligands and the high shift of binding energy to N–O···H (532.9 eV). Meanwhile, the other parts of amidoxime groups were hindered by steric effect and failed to interact with *ortho*-amino (Fig. S1(b) in the ESM), bringing about high system energy and lower binding energy of $N–O_{st}$ species to 531.4 eV [44]. The differentiated states of oxime groups are associated with the potential multiple coordination modes of CMP-mAO-oNH_2 to uranyl ions. In addition, the C 1s region of amidoxime CMPs was fit with three peaks assigned to C–N/C–O (286.4 eV), C=N (285.4 eV), and C=C/C≡C (284.6 eV), as shown in Fig. 2(c). The spectra of C 1s present no significant changes except a slight increase of C–N/C–O signal for CMP-mAO-oNH_2, indicating the amino functionalities while confirming the stability of CMPs skeleton. The high-resolution C 1s and O 1s regions with deconvolution analysis of CMPs before amidoximation were also provided for comparison in Fig. S2 in the ESM.

The porous properties of CMPs were evaluated by N_2 sorption–desorption experiment. Figures 3(a) and 3(b) give the isotherms comparison of CMPs before and after amidoximation while Table 3 summarizes the porosity parameters. The CMP-mCN sample exhibits a combination of type I and type IV isotherms, which illustrates a combination of monolayer adsorption with a finite multi-layer formation corresponding to complete filling of the capillaries in CMP-mCN. The rapid uptake of N_2 at low relative pressure and hysteresis at medium relative pressure indicates the coexistence of micro- and mesopores in CMP-mCN, showing complex hierarchical porosity and a BET specific surface area of 676 m^2/g. With the conversion of nitrile to amidoxime, the isotherm remains the original type, suggesting an intact porous structure. Due to the formation of large-sized amidoxime functionalities in the pores, the BET specific surface area of CMP-mAO decreases to 235 m^2/g. In the case of CMPs with ortho-substituted amino groups, the isotherms present more irreversible adsorption features that can be attributed to the existence of more small micropores component and a kinetic barrier of adsorption [57, 58]. The BET specific surface areas of CMP-mCN-oNH_2 and CMP-mAO-oNH_2 were calculated to be 325 and 101 m^2/g, respectively, giving a

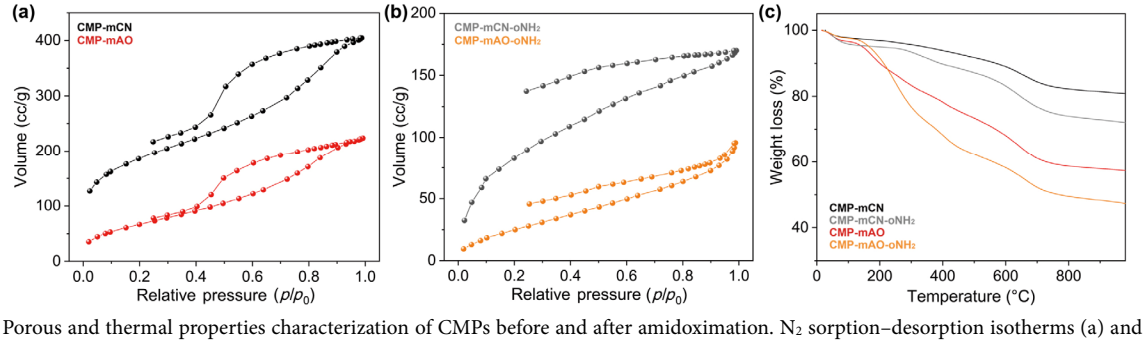

Figure 3 Porous and thermal properties characterization of CMPs before and after amidoximation. N_2 sorption–desorption isotherms (a) and (b), TGA curves (c).

Table 3 Porosity parameters of CMPs before and after amidoximation

Sample	Porosity parameters	
	Specific surface area (m^2/g)	Pore volume (cm^3/g)
CMP-mCN	676	0.626
CMP-mAO	235	0.263
CMP-mCN-oNH$_2$	325	0.346
CMP-mAO-oNH$_2$	101	0.148

notable decrease compared with their amino-free counterparts. The pore size distribution of CMPs before amidoximation (Fig. S3 in the ESM) was calculated by using the nonlocal density functional theory (NLDFT), which gives well-developed hierarchically porous structures beneficial to mass transport and improves the adsorption capacity of sorbents [59]. SEM images show rough surface composed of all CMPs (Fig. S4 in the ESM), suggesting the structural integrity during amidoximation process.

The thermal stability of CMPs was investigated by TGA as shown in Fig. 3(c). A slight weight loss under 100 °C in all CMPs samples can be ascribed to the removal of small molecular adsorbates or residues during synthesis. The CMPs-mCN exhibits relatively high thermal stability with a decomposition temperature (T_d) around 250 °C. With the introduction of amino group and conversion of cyano to amidoxime, the content of functional groups with relatively poor thermostability increased, resulting in the increase of weight loss and the decrease of T_d.

To explore the potential synergistic effect of *ortho*-substituted amino to amidoxime, the adsorption behavior of CMP-mAO and CMP-mAO-oNH$_2$ toward uranyl ions in aqueous solutions was studied in a series of batch experiments. Figure 4(a) demonstrates the effect of pH, ranging from 2 to 7, on the uranyl ions adsorption efficiency of amidoxime CMPs. The CMPs showed peak values of adsorption capacity at pH 6. Such an optimal pH is generally obtained for uranium adsorption by amidoxime functionalized sorbents, which benefits the deprotonation of amidoxime functional groups while preventing the hydrolyzation of uranium species [60]. The adsorption capacity of uranyl ions by amidoxime CMPs as a function of equilibrium concentration (C_e) in solution was obtained to investigate the adsorption isotherm (Fig. 4(b)), where the initial concentrations of uranium were varied from 10 to 200 mg/L. The Langmuir and Freundlich adsorption isotherm models were employed to fit the experimental data with the parameters listed in Table S1 in the ESM. With the tendency of adsorption capacity increasing rapidly at low C_e and approaching to the equilibrium at high C_e, it is evident that the Langmuir model gives a better fitting result for both amidoxime CMPs with a higher correlation coefficient R^2, implying a monolayer adsorption process via the coordination of uranyl ions with adsorption site on CMPs [61]. The saturation adsorption capacity of CMP-mAO-oNH$_2$ estimated by Langmuir model was about 174 mg/g, significantly improved than that of CMP-mAO (105 mg/g). With the theoretical values of functional group content, the percentage of amidoxime in CMPs engaged in the coordination to uranium was increased from 12.3% to 21.7% in 1:1 M/L coordination mode. Moreover, the variation of adsorption amount upon contact time was also carried out at the initial concentration of uranyl ions of 20 mg/L. The kinetic curve in Fig. 4(c) shows an obvious difference between two amidoxime CMPs, where CMP-mAO-oNH$_2$ presents faster adsorption kinetics but never approaching equilibrium within the experimental time. Three kinetic models, i.e. pseudo-first-order, pseudo-second-order, and Weber-Morris model, were used to fit the kinetic experimental data (Table S2 in the ESM), from which the Weber-Morris intra-particle diffusion model fits well with the adsorption procedure for both amidoxime CMPs [62]. Such kinetic behavior can be attributed to the limited diffusion of uranyl ions in the complex hierarchical pore structures of CMPs, indicating that the intra-particle diffusion acts as the rate-determining step of the adsorption process [63]. All the above adsorption behaviors demonstrate that the introduction of synergistic amino functionalities at *ortho*-position to amidoxime evidently promotes the performance of the CMPs for adsorption of uranyl ions.

To further investigate the synergistic effect of *ortho*-amino and reveal the adsorption mechanism of uranyl ions on amidoxime CMPs, the amidoxime CMPs and their counterparts after exposure to uranium solution were examined by detailed analysis of the XPS spectra. All the samples were washed by deionized water and dried under vacuum before analysis to eliminate the interference of weak interactions. The adsorbed uranyl ions on amidoxime CMPs were evidenced by the appearance of U 4f signal at 393 and 382 eV in wide scan XPS spectra (Fig. 5(a)) and high-resolution XPS spectra of U 4f region (Fig. S5 in the ESM). The U 4f intensity of CMP-mAO-oNH$_2$-U is distinctly stronger than that of CMP-mAO-U, indicating the relatively high adsorption amount and strong interaction. High-resolution N 1s and O 1s regions with deconvolution analysis are presented in Figs. 5(b) and 5(c). Likewise, the N 1s region (Fig. 5(b)) can be fitted with two components assigned to –NH$_2$ and =N– species. In the case of CMP-mAO-U, after binding to uranyl ions, the peak of =N– shows a shift of 0.2 eV to relatively higher binding energy while the –NH$_2$ presents no significant change. Since the shift of binding energy reflects the change in a local chemical environment or electron density of atoms in corresponding species [64, 65], these phenomena imply that the oxime group

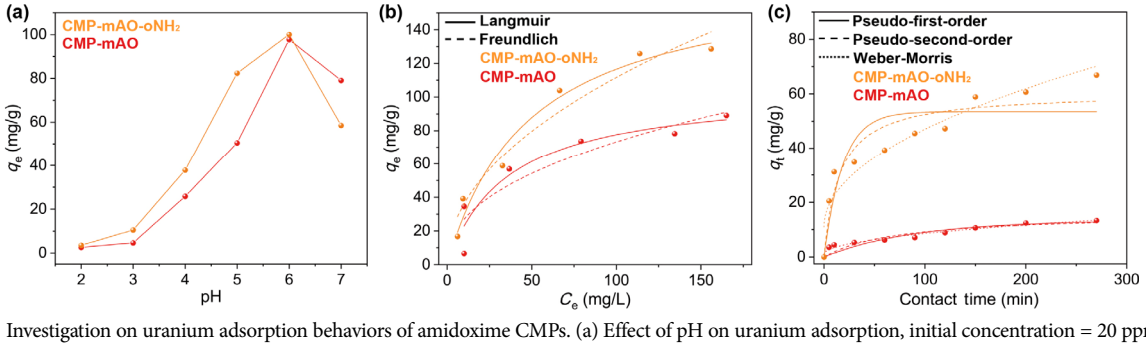

Figure 4 Investigation on uranium adsorption behaviors of amidoxime CMPs. (a) Effect of pH on uranium adsorption, initial concentration = 20 ppm, contact time = 3 h, [m/V] ~ 0.2 g/L; (b) uranium adsorption isotherm fitted by the Langmuir model and Freundlich model, contact time = 5 h, [m/V] ~ 0.4 g/L; (c) uranium adsorption kinetics curves fitted by the pseudo-first-order, pseudo-second-order and Weber-Morris model, initial concentration = 20 ppm, [m/V] ~ 0.02 g/L.

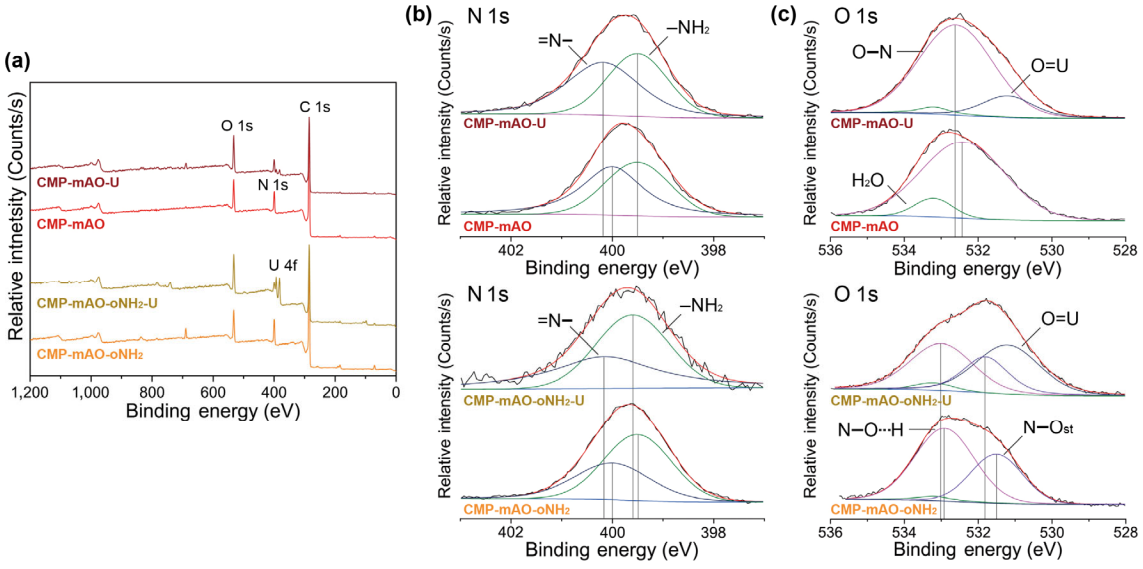

Figure 5 Wide scan XPS spectra (a), high-resolution XPS spectra of N 1s (b) and O 1s (c) regions for amidoxime CMPs before and after uranium adsorption, CMP-mAO-U (wine), CMP-mAO-oNH$_2$-U (wheat).

in amidoxime plays a vital role in coordination with uranyl ions but the amino group of amidoxime might be not involved, suggesting the preferential coordination model [38]. As for CMP-mAO-oNH$_2$-U, the *ortho*-amino on aromatic ring takes part in the coordination of oxime with uranyl ions, giving a movement of –NH$_2$ signal about 0.1 eV to the higher binding energy. The O 1s region (Fig. 5(c)) also reflects the coordinate behavior of amidoxime CMPs to uranyl ions. After exposure to uranium solution, evident uranyl ions peak (O=U species) at 531.2 eV appears for both samples, confirming the adsorption of uranium on CMPs. In addition, all types of O–N species, including disproportionated hydrogen bond type (N–O···H) and steric hindrance type (N–O$_{st}$), shift more or less to relatively higher binding energy region, implying all types of O–N species were involved in the coordination with uranyl ions.

The underlying coordination mechanism involving the synergistic binding of uranyl ions by the amidoxime-functionalized CMPs with *ortho*-substituted amino is probed based on DFT calculation. The expanded boundless CMPs were replaced by the *ortho*-amino-benzamidoxime model ligands as a single moiety, giving four rational coordination modes including M/L of 1:1 and 1:2 species presented in Fig. 6. Basically, the amino at *ortho*-position may potentially interact with uranyl ions in either direct synergistic coordination mode (Figs. 6(a) and 6(b)) or secondary-sphere interaction mode (Figs. 6(c) and 6(d)). DFT calculation was employed to optimize the coordination interactions for identifying the most energetically favored modes. In the cases of direct synergistic coordination mode, the reaction energies (ΔE) were calculated to be −144.3 and −251.0 kcal/mol for the 1:1 and 1:2 M/L modes, respectively. Though the 1:2 M/L coordination mode represents a more thermodynamically stable state, it is unlikely to be formed due to the conformational and space hindrance in the confined pore channels of CMPs with rigid skeletons. Thus, 1:1 M/L coordination should be the dominant mode. The optimized structure of the 1:1 M/L mode shows the angles of axial U=O bond in uranyl ion squeezed from 180° to around 150° (Figs. 6(a) and 6(c)), suggesting the strong binding of amidoxime ligands and the synergistic amino functionalities to uranyl ions in the equatorial plane. For secondary-sphere interaction mode, the distance between the amino groups at *ortho*-position and adjacent hydrogen in bound water of uranyl was calculated to be around 1.8 Å (marked by orange

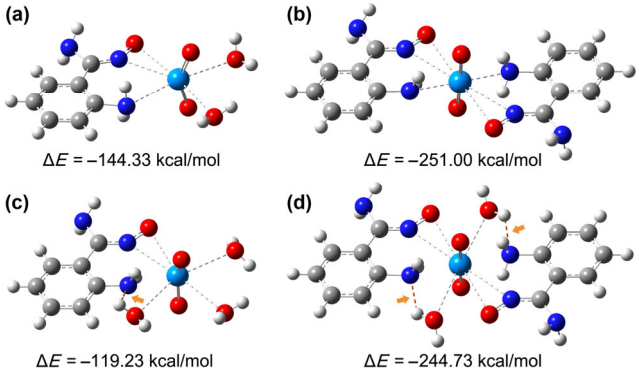

Figure 6 Optimized structures and reaction energies for uranyl/*ortho*-amino-benzamidoxime complexes taking different coordination modes. Direct synergistic coordination mode: M/L = 1:1 (a), M/L = 1:2 (b); secondary-sphere interaction mode: M/L = 1:1 (c), M/L = 1:2 (d).

arrows in Fig. 6), which is in the scope of hydrogen bond interaction. For a 1:1 M/L coordination mode with the uranyl/*ortho*-amino-benzamidoxime complex stabilized by second sphere hydrogen bonding interactions [28], the reaction energy ΔE was calculated to be −119.2 kcal/mol, indicating that the secondary-sphere interaction mode is less stable than the direct synergistic coordination mode. Therefore, the results of DFT calculation suggest that the optimal coordination mechanism in CMPs-mAO-oNH$_2$ is the 1:1 M/L coordination mode stabilized by the direct synergistic effect of the *ortho*-substituted amino functionalities. However, considering the same order of magnitude for the reaction energies of the two modes, there still exists the possibility of secondary-sphere interaction. Overall, the CMP sorbents synthesized by the *de novo* synthetic strategy demonstrated an evidently enhanced capability for uranyl ions entrapment by taking advantage of the synergistic effect. Meanwhile, their hierarchical frameworks with well-developed pore channels resulted in an intra-particle diffusion-limited adsorption kinetics process.

4 Conclusions

In this work, a novel class of CMPs bearing amidoxime and synergistic functionalities were developed by a *de novo* synthetic method using the Sonogashira-Hagihara coupling reaction.

The CMPs possessed rich functional groups, high specific surface area, well-developed porosity, and structural advantages in terms of chemical and thermal stability. By taking advantage of the electron-donating amino functionalities specifically located at the *ortho*-position to the amidoxime groups, synergistic binding of uranyl ions was achieved, showing a significantly increased adsorption capacity ~ 174 mg/g. New insights into the coordination mechanism of the bifunctional CMPs to uranyl ions were revealed by XPS analysis and DFT calculation. The amidoxime groups were mainly responsible for the binding of uranyl ions, while the *ortho*-substituted amino functionalities synergistically stabilized the 1:1 M/L complexes by direct interaction with the uranium centers or participated in the coordination via hydrogen bonding involved secondary-sphere interaction. In summary, this study provided a new methodology for task-specific design and synthesis of bifunctional CMP sorbents and shed light on the underlying principles of *ortho*-functionality involved synergistic effect in uranium coordination.

Acknowledgements

The study was financially supported by the National Natural Science Foundation of China (Nos. 21922604 and 51673109) and Innovative Research Team in University (No. IRT13026). Partial support from the U.S. National Science Foundation (No. CBET-1706025) and the Robert A. Welch Foundation (No. B-0027) is also acknowledged (S. Q. M.).

Electronic Supplementary Material: Supplementary material (molecular structure, XPS, pore size distribution, SEM, and fitting parameters) is available in the online version of this article at https://doi.org/10.1007/s12274-020-3217-7.

References

[1] Das, S.; Heasman, P.; Ben, T.; Qiu, S. L. Porous organic materials: Strategic design and structure-function correlation. *Chem. Rev.* **2017**, *117*, 1515–1563.

[2] Holst, J. R.; Stöckel, E.; Adams, D. J.; Cooper, A. I. High surface area networks from tetrahedral monomers: Metal-catalyzed coupling, thermal polymerization, and "click" chemistry. *Macromolecules* **2010**, *43*, 8531–8538.

[3] Sonogashira, K.; Tohda, Y.; Hagihara, N. A convenient synthesis of acetylenes: Catalytic substitutions of acetylenic hydrogen with bromoalkenes, iodoarenes and bromopyridines. *Tetrahedron Lett.* **1975**, *16*, 4467–4470.

[4] Jiang, J. X.; Su, F. B.; Trewin, A.; Wood, C. D.; Campbell, N. L.; Niu, H. J.; Dickinson, C.; Ganin, A. Y.; Rosseinsky, M. J.; Khimyak, Y. Z. et al. Conjugated microporous poly(aryleneethynylene) networks. *Angew. Chem., Int. Ed.* **2007**, *46*, 8574–8578.

[5] Cooper, A. I. Conjugated microporous polymers. *Adv. Mater.* **2009**, *21*, 1291–1295.

[6] Meng, Z.; Mirica, K. A. Two-dimensional d-π conjugated metal-organic framework based on hexahydroxytrinaphthylene. *Nano Res.* **2021**, *14*, 369–375.

[7] Xu, Y. H.; Chen, L.; Guo, Z. Q.; Nagai, A.; Jiang, D. L. Light-emitting conjugated polymers with microporous network architecture: Interweaving scaffold promotes electronic conjugation, facilitates exciton migration, and improves luminescence. *J. Am. Chem. Soc.* **2011**, *133*, 17622–17625.

[8] Liu, H. Q.; Wang, Y.; Mo, W. Q.; Tang, H. L.; Cheng, Z. Y.; Chen, Y.; Zhang, S. T.; Ma, H. W.; Li, B.; Li, X. B. Dendrimer-based, high-luminescence conjugated microporous polymer films for highly sensitive and selective volatile organic compound sensor arrays. *Adv. Funct. Mater.* **2020**, *30*, 1910275.

[9] Zhou, Y. B.; Zhan, Z. P. Conjugated microporous polymers for heterogeneous catalysis. *Chem.—Asian J.* **2018**, *13*, 9–19.

[10] Liu, M. X.; Zhou, B. L.; Zhou, L.; Xie, Z.; Li, S.; Chen, L. Nitroxyl radical based conjugated microporous polymers as heterogeneous catalysts for selective aerobic alcohol oxidation. *J. Mater. Chem. A* **2018**, *6*, 9860–9865.

[11] Liao, Y. Z.; Wang, H. G.; Zhu, M. F.; Thomas, A. Efficient supercapacitor energy storage using conjugated microporous polymer networks synthesized from Buchwald–Hartwig coupling. *Adv. Mater.* **2018**, *30*, 1705710.

[12] Lee, J. S. M.; Wu, T. H.; Alston, B. M.; Briggs, M. E.; Hasell, T.; Hu, C. C.; Cooper, A. I. Porosity-engineered carbons for supercapacitive energy storage using conjugated microporous polymer precursors. *J. Mater. Chem. A* **2016**, *4*, 7665–7673.

[13] Ren, Y. M.; Yu, C. B.; Chen, Z. H.; Xu, Y. X. Two-dimensional polymer nanosheets for efficient energy storage and conversion. *Nano Res.* in press, DOI: 10.1007/s12274-020-2976-5.

[14] Liu, Y. C.; Cui, Y. Z.; Zhang, C. H.; Du, J. F.; Wang, S.; Bai, Y.; Liang, Z. Q.; Song, X. W. Post-cationic modification of a pyrimidine-based conjugated microporous polymer for enhancing the removal performance of anionic dyes in water. *Chem.—Eur. J.* **2018**, *24*, 7480–7488.

[15] A, S.; Zhang, Y. W.; Li, Z. P.; Xia, H.; Xue, M.; Liu, X. M.; Mu, Y. Highly efficient and reversible iodine capture using a metalloporphyrin-based conjugated microporous polymer. *Chem. Commun.* **2014**, *50*, 8495–8498.

[16] Yang, C. H.; Li, S. Y.; Zhang, Z. C.; Wang, H. Q.; Liu, H. L.; Jiao, F.; Guo, Z. G.; Zhang, X. T.; Hu, W. P. Organic-inorganic hybrid nanomaterials for electrocatalytic CO_2 reduction. *Small* **2020**, *16*, 2001847.

[7] Xiang, L.; Zhu, Y. L.; Gu, S.; Chen, D. Y.; Fu, X.; Zhang, Y. D.; Yu, G. P.; Pan, C. Y.; Hu, Y. H. A luminescent hypercrosslinked conjugated microporous polymer for efficient removal and detection of mercury ions. *Macromol. Rapid Commun.* **2015**, *36*, 1566–1571.

[18] Yang, S.; Cao, Y.; Wang, T.; Cai, S. Y.; Xu, M. Y.; Lu, W. H.; Hua, D. B. Positively charged conjugated microporous polymers with antibiofouling activity for ultrafast and highly selective uranium extraction from seawater. *Environ. Res.* **2020**, *183*, 109214.

[19] Slater, A. G.; Cooper, A. I. Function-led design of new porous materials. *Science* **2015**, *348*, aaa8075.

[20] Chen, J.; Yan, W.; Townsend, E. J.; Feng, J. T.; Pan, L.; Del Angel Hernandez, V.; Faul, C. F. J. Tunable surface area, porosity, and function in conjugated microporous polymers. *Angew. Chem., Int. Ed.* **2019**, *58*, 11715–11719.

[21] Xu, Y. H.; Jin, S. B.; Xu, H.; Nagai, A.; Jiang, D. L. Conjugated microporous polymers: Design, synthesis and application. *Chem. Soc. Rev.* **2013**, *42*, 8012–8031.

[22] Zhou, L.; Bosscher, M.; Zhang, C. S.; Özçubukçu, S.; Zhang, L.; Zhang, W.; Li, C. J.; Liu, J. Z.; Jensen, M. P.; Lai, L. H. et al. A protein engineered to bind uranyl selectively and with femtomolar affinity. *Nat. Chem.* **2014**, *6*, 236–241.

[23] Sun, Q.; Aguila, B.; Song, Y. P.; Ma, S. Q. Tailored porous organic polymers for task-specific water purification. *Acc. Chem. Res.* **2020**, *53*, 812–821.

[24] Xie, Y.; Chen, C. L.; Ren, X. M.; Wang, X. X.; Wang, H. Y.; Wang, X. K. Emerging natural and tailored materials for uranium-contaminated water treatment and environmental remediation. *Prog. Mater. Sci.* **2019**, *103*, 180–234.

[25] Gill, G. A.; Kuo, L. J.; Janke, C. J.; Park, J.; Jeters, R. T.; Bonheyo, G. T.; Pan, H. B.; Wai, C.; Khangaonkar, T.; Bianucci, L. et al. The uranium from seawater program at the pacific northwest national laboratory: Overview of marine testing, adsorbent characterization, adsorbent durability, adsorbent toxicity, and deployment studies. *Ind. Eng. Chem. Res.* **2016**, *55*, 4264–4277.

[26] Chu, S.; Majumdar, A. Opportunities and challenges for a sustainable energy future. *Nature* **2012**, *488*, 294–303.

[27] Sun, Q.; Aguila, B.; Ma, S. Q. Opportunities of porous organic polymers for radionuclide sequestration. *Trends Chem.* **2019**, *1*, 292–303.

[28] Odoh, S. O.; Bondarevsky, G. D.; Karpus, J.; Cui, Q.; He, C.; Spezia, R.; Gagliardi, L. UO_2^{2+} uptake by proteins: Understanding the binding features of the super uranyl binding protein and design of a protein with higher affinity. *J. Am. Chem. Soc.* **2014**, *136*, 17484–17494.

[29] Li, B. Y.; Sun, Q.; Zhang, Y. M.; Abney, C. W.; Aguila, B.; Lin, W. B.; Ma, S. Q. Functionalized porous aromatic framework for efficient uranium adsorption from aqueous solutions. *ACS Appl. Mater. Interfaces* **2017**, *9*, 12511–12517.

[30] Xu, M. Y.; Han, X. L.; Wang, T.; Li, S. H.; Hua, D. B. Conjugated microporous polymers bearing phosphonate ligands as an efficient sorbent for potential uranium extraction from high-level liquid wastes. *J. Mater. Chem. A* **2018**, *6*, 13894–13900.

[31] Wang, T.; Xu, M. Y.; Han, X. L.; Yang, S.; Hua, D. B. Petroleum pitch-based porous aromatic frameworks with phosphonate ligand for efficient separation of uranium from radioactive effluents. *J. Hazard. Mater.* **2019**, *368*, 214–220.

[32] Kiskan, B.; Weber, J. Versatile postmodification of conjugated microporous polymers using thiol-yne chemistry. *ACS Macro Lett.* **2011**, *1*, 37–40.

[33] Abney, C. W.; Mayes, R. T.; Saito, T.; Dai, S. Materials for the recovery of uranium from seawater. *Chem. Rev.* **2017**, *117*, 13935–14013.

[34] Aguila, B.; Sun, Q.; Cassady, H.; Abney, C. W.; Li, B. Y.; Ma, S. Q. Design strategies to enhance amidoxime chelators for uranium recovery. *ACS Appl. Mater. Interfaces* **2019**, *11*, 30919–30926.

[35] Sun, Q.; Aguila, B.; Earl, L. D.; Abney, C. W.; Wojtas, L.; Thallapally, P. K.; Ma, S. Q. Covalent organic frameworks as a decorating platform for utilization and affinity enhancement of chelating sites for radionuclide sequestration. *Adv. Mater.* **2018**, *30*, 1705479.

[36] Tian, G. X.; Teat, S. J.; Zhang, Z. Y.; Rao, L. F. Sequestering uranium from seawater: Binding strength and modes of uranyl complexes with glutarimidedioxime. *Dalton Trans.* **2012**, *41*, 11579–11586.

[37] Eloy, F.; Lenaers, R. The chemistry of amidoximes and related compounds. *Chem. Rev.* **1962**, *62*, 155–183.

[38] Kelley, S. P.; Barber, P. S.; Mullins, P. H. K.; Rogers, R. D. Structural clues to UO_2^{2+}/VO_2^+ competition in seawater extraction using amidoxime-based extractants. *Chem. Commun.* **2014**, *50*, 12504–12507.

[39] Vukovic, S.; Watson, L. A.; Kang, S. O.; Custelcean, R.; Hay, B. P. How amidoximate binds the uranyl cation. *Inorg. Chem.* **2012**, *51*, 3855–3859.

[40] Zhang, A. Y.; Asakura, T.; Uchiyama, G. The adsorption mechanism of uranium(VI) from seawater on a macroporous fibrous polymeric adsorbent containing amidoxime chelating functional group. *React. Funct. Polym.* **2003**, *57*, 67–76.

[41] Zhang, L.; Pu, N.; Yu, B. X.; Ye, G.; Chen, J.; Xu, S. M.; Ma, S. Q. Skeleton engineering of homocoupled conjugated microporous polymers for highly efficient uranium capture via synergistic coordination. *ACS Appl. Mater. Interfaces* **2020**, *12*, 3688–3696.

[42] Vukovic, S.; Hay, B. P. *De novo* structure-based design of bis-amidoxime uranophiles. *Inorg. Chem.* **2013**, *52*, 7805–7810.

[43] Bai, C. Y.; Zhang, M. C.; Li, B.; Zhao, X. S.; Zhang, S.; Wang, L.; Li, Y.; Zhang, J.; Ma, L. J.; Li, S. J. Modifiable diyne-based covalent organic framework: A versatile platform for *in situ* multipurpose functionalization. *RSC Adv.* **2016**, *6*, 39150–39158.

[44] Sun, Q.; Aguila, B.; Perman, J.; Ivanov, A. S.; Bryantsev, V. S.; Earl, L. D.; Abney, C. W.; Wojtas, L.; Ma, S. Q. Bio-inspired nano-traps for uranium extraction from seawater and recovery from nuclear waste. *Nat. Commun.* **2018**, *9*, 1644.

[45] Xu, M. Y.; Wang, T.; Gao, P.; Zhao, L.; Zhou, L.; Hua, D. B. Highly fluorescent conjugated microporous polymers for concurrent adsorption and detection of uranium. *J. Mater. Chem. A* **2019**, *7*, 11214–11222.

[46] Xiong, J.; Hu, S.; Liu, Y.; Yu, J.; Yu, H. Z.; Xie, L.; Wen, J.; Wang, X. L. Polypropylene modified with amidoxime/carboxyl groups in separating uranium(VI) from thorium(IV) in aqueous solutions. *ACS Sustainable Chem. Eng.* **2017**, *5*, 1924–1930.

[47] Alexandratos, S. D.; Zhu, X. P.; Florent, M.; Sellin, R. Polymer-supported bifunctional amidoximes for the sorption of uranium from seawater. *Ind. Eng. Chem. Res.* **2016**, *55*, 4208–4216.

[48] Wei, Y. Q.; Qian, J.; Huang, L.; Hua, D. B. Bifunctional polymeric microspheres for efficient uranium sorption from aqueous solution: Synergistic interaction of positive charge and amidoxime group. *RSC Adv.* **2015**, *5*, 64286–64292.

[49] Zhang, Y.; Zhang, Y.; Sun, Y. L.; Du, X.; Shi, J. Y.; Wang, W. D.; Wang, W. 4-(*N,N*-Dimethylamino)pyridine-embedded nanoporous conjugated polymer as a highly active heterogeneous organocatalyst. *Chem. –Eur. J.* **2012**, *18*, 6328–6334.

[50] Bai, Z. Q.; Yuan, L. Y.; Zhu, L.; Liu, Z. R.; Chu, S. Q.; Zheng, L. R.; Zhang, J.; Chaid, Z. F.; Shi, W. Q. Introduction of amino groups into acid-resistant mofs for enhanced U(VI) sorption. *J. Mater. Chem. A* **2015**, *3*, 525–534.

[51] Alkordi, M. H.; Haikal, R. R.; Hassan, Y. S.; Emwas, A. H.; Belmabkhout, Y. Poly-functional porous-organic polymers to access functionality—CO_2 sorption energetic relationships. *J. Mater. Chem. A* **2015**, *3*, 22584–22590.

[52] Jiang, J. X.; Su, F. B.; Trewin, A.; Wood, C. D.; Niu, H. J.; Jones, J. T. A.; Khimyak, Y. Z.; Cooper, A. I. Synthetic control of the pore dimension and surface area in conjugated microporous polymer and copolymer networks. *J. Am. Chem. Soc.* **2008**, *130*, 7710–7720.

[53] Pan, H. B.; Kuo, L. J.; Wood, J.; Strivens, J.; Gill, G. A.; Janke, C. J.; Wai, C. M. Towards understanding KOH conditioning of amidoxime-based polymer adsorbents for sequestering uranium from seawater. *RSC Adv.* **2015**, *5*, 100715–100721.

[54] Das, S.; Brown, S.; Mayes, R. T.; Janke, C. J.; Tsouris, C.; Kuo, L. J.; Gill, G.; Dai, S. Novel poly(imide dioxime) sorbents: Development and testing for enhanced extraction of uranium from natural seawater. *Chem. Eng. J.* **2016**, *298*, 125–135.

[55] Yu, Z. J.; Kang, E. T.; Neoh, K. G. Amidoximation of the acrylonitrile polymer grafted on poly(tetrafluoroethylene-co-hexafluoropropylene) films and its relevance to the electroless plating of copper. *Langmuir* **2002**, *18*, 10221–10230.

[56] Omichi, H.; Katakai, A.; Sugo, T.; Okamoto, J. A new type of amidoxime-group-containing adsorbent for the recovery of uranium from seawater. *Sep. Sci. Technol.* **1985**, *20*, 163–178.

[57] Ju, P. Y.; Wu, S. J.; Su, Q.; Li, X. D.; Liu, Z. Q.; Li, G. H.; Wu, Q. L. Salen–porphyrin-based conjugated microporous polymer supported pd nanoparticles: Highly efficient heterogeneous catalysts for aqueous C–C coupling reactions. *J. Mater. Chem. A* **2019**, *7*, 2660–2666.

[58] Xu, C.; Hedin, N. Synthesis of microporous organic polymers with high CO_2-over-N_2 selectivity and co_2 adsorption. *J. Mater. Chem. A* **2013**, *1*, 3406–3414.

[59] Sun, M. H.; Huang, S. Z.; Chen, L. H.; Li, Y.; Yang, X. Y.; Yuan, Z. Y.; Su, B. L. Applications of hierarchically structured porous materials from energy storage and conversion, catalysis, photocatalysis, adsorption, separation, and sensing to biomedicine. *Chem. Soc. Rev.* **2016**, *45*, 3479–3563.

[60] Yang, Y.; Wang, J. C.; Wu, F. C.; Ye, G.; Yi, R.; Lu, Y. X.; Chen, J. Surface-initiated SET-LRP mediated by mussel-inspired polydopamine chemistry for controlled building of novel core–shell magnetic nanoparticles for highly-efficient uranium enrichment. *Polym. Chem.* **2016**, *7*, 2427–2435.

[61] Wu, F. C.; Ye, G.; Liu, Y. K.; Yi, R.; Huo, X. M.; Lu, Y. X.; Chen, J. New short-channel SBA-15 mesoporous silicas functionalized with polyazamacrocyclic ligands for selective capturing of palladium ions in HNO_3 media. *RSC Adv.* **2016**, *6*, 66537–66547.

[62] Doğan, M.; Abak, H.; Alkan, M. Adsorption of methylene blue onto hazelnut shell: Kinetics, mechanism and activation parameters. *J. Hazard. Mater.* **2009**, *164*, 172–181.

[63] Zhang, S.; Zhao, X. S.; Li, B.; Bai, C. Y.; Li, Y.; Wang, L.; Wen, R.; Zhang, M. C.; Ma, L. J.; Li, S. J. "Stereoscopic" 2D super-microporous phosphazene-based covalent organic framework: Design, synthesis and selective sorption towards uranium at high acidic condition. *J. Hazard. Mater.* **2016**, *314*, 95–104.

[64] Wu, F. C.; Ye, G.; Yi, R.; Sun, T. X.; Xu, C.; Chen, J. Novel polyazamacrocyclic receptor decorated core-shell superparamagnetic microspheres for selective binding and magnetic enrichment of palladium: Synthesis, adsorptive behavior and coordination mechanism. *Dalton Trans.* **2016**, *45*, 9553–9564.

[65] Stevens, J. S.; de Luca, A. C.; Pelendritis, M.; Terenghi, G.; Downes, S.; Schroeder, S. L. M. Quantitative analysis of complex amino acids and RGD peptides by X-ray photoelectron spectroscopy (XPS). *Surf. Interface Anal.* **2013**, *45*, 1238–1246.